An Enhanced One-Layer Passive Microfluidic Mixer With an Optimized Lateral Structure With the Dean Effect

4 authors, including:

Teng Zhou
Hainan University
4 PUBLICATIONS **9** CITATIONS

SEE PROFILE

Zhenyu Liu
Changchun Institute of Optics, Fine Mechani...
63 PUBLICATIONS **332** CITATIONS

SEE PROFILE

Teng Zhou
School of Mechanical Engineering,
Yeungnam University,
Gyeongsan 712-749, South Korea

Yifan Xu
Changchun Institute of Optics
Fine Mechanics and Physics (CIOMP),
Chinese Academy of Science,
Changchun, Jilin 130033, China

Zhenyu Liu
Changchun Institute of Optics
Fine Mechanics and Physics (CIOMP),
Chinese Academy of Science,
Changchun, Jilin 130033, China

Sang Woo Joo[1]
School of Mechanical Engineering,
Yeungnam University,
Gyeongsan 712-749, South Korea
e-mail: swjoo@yu.ac.kr

An Enhanced One-Layer Passive Microfluidic Mixer With an Optimized Lateral Structure With the Dean Effect

Topology optimization method is applied to a contraction–expansion structure, based on which a simplified lateral flow structure is generated using the Boolean operation. A new one-layer mixer is then designed by sequentially connecting this lateral structure and bent channels. The mixing efficiency is further optimized via iterations on key geometric parameters associated with the one-layer mixer designed. Numerical results indicate that the optimized mixer has better mixing efficiency than the conventional contraction–expansion mixer for a wide range of the Reynolds number. [DOI: 10.1115/1.4030288]

1 Introduction

Efficient reagent mixing continues to be of great importance in many biochemical processes requiring even reactions between ingredients [1–4]. However, mixing of fluids usually relies mainly on the diffusion and the convection effects, which become weak in microscale [5,4]. In microfluidic channels, the flow is usually laminar [6–9], and an efficient mixing can be hard to realize. Many microfluidic mixers are thus proposed to shorten the mixing distance and enhance the diffusion length.

Microfluidic mixers are often classified into two types: passive and active types. An active mixer uses an external energy source, such as electric [2,10], magnetic [11–13], and acoustic [14] fields, to enhance the turbulence in the fluid, which can sometimes damage delicate biological cells. A passive mixer, on the other hand, uses geometrical variation in the channel structure, inducing complex fluid motion to achieve an appropriate mixing [4]. Such a mixer thus can have a better bioviability and easier integrability, among other advantages.

Many different structures with different passive effects are proposed to mix microfluidic reagents and particles [3,15–18]. The Dean-force mixer, for example, uses the curvature of a channel to generate the Dean force. The split-and-recombination channel generates chaotic flow for mixing samples [3,15,]. In Dean-force mixers, Dean number beyond a threshold value needs to be maintained for efficiency, and thus serpentine structures are usually used to maintain a certain curvature in most of the channel [16–18]. Lee et al. propose a contraction–expansion array (CEA), which can be used to generate the Dean vortex [19–22], as shown in Fig. 1. The intersection of the CEA structure has an abrupt change before the expansion structure, and generates the Dean vortex helping the two samples envelop each other. This phenomenon enhances the diffusion and convection effects in the fluid.

In the present study, the passive mixer is further enhanced by utilizing the topology optimization method [23–25] for higher efficiency for a wide range of the Reynolds number used in microfluidic mixers. Based on the optimization result, we propose a lateral structure, which is then used in the one-layer mixer developed as a more efficient and versatile alternative. The remainder of the paper is organized as follows: The optimization theory and the computational method are provided in Sec. 2. In Sec. 3, a lateral structure is proposed based on the optimization result. The principle associated with the lateral structure and the mixer is also specified. In Sec. 4, we perform a parametric study to configure the arrangements of the lateral structure. It will be shown that a serpentine-structure chip with period of one lateral structure exhibits good performance in a wide range of the Reynolds number. The new lateral structural and the original mixer are compared, and optimization on the channel aspect ratio is also performed.

2 Topology Optimization of Contraction–Expansion Unit

2.1 Optimization Model. The mixing effect of the two flows with an anticipated distribution of the concentration at the outlet can be expressed using the least-square type optimization objective as [19,24]
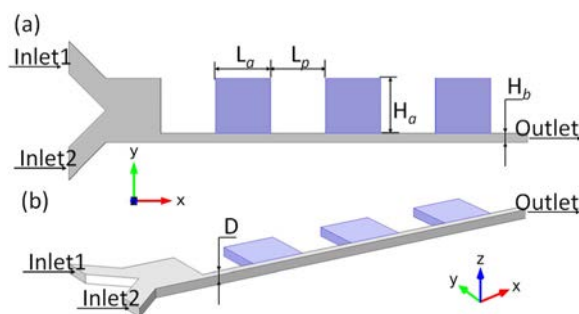
Fig. 1 Schematic of CAE in (*a*) front view and (*b*) Isometric drawing. Blue shade shows the optimization domain. H_a: width of expansion domain; L_a: length of expansion domain; L_p: distance between the periods of the mixer; H_b: width of contraction domain; and D: channel depth.

$$\sigma = \frac{\int_{\Gamma}(c-\bar{c})^2}{A\bar{c}^2} \tag{1}$$

where c is the concentration of the reagent, $\bar{c}$ denotes the average concentration, Γ is the cross plane from which we measure the concentration, A is the area of the cross plane. Complete mixing and complete segregation are then defined by $\sigma = 0$ and $\sigma = 1$, respectively. The lower the value is, therefore, the better is the performance of the mixer.

The design goal of the topology optimization is to find a reasonable layout of fluidic channels corresponding to the lowest value of the mixing measurement in a specified design domain. Under the hypothesis of continuum, microfluidic flow is described by the nonlinearly coupled system of conservation of momentum, mass, and species, where the first two of which are described here by the steady Navier–Stokes equations and the continuity equation for incompressible fluids, and the conservation of species is described by the steady convection–diffusion equation. In the topology optimization method, which was proposed by Borrvall and Petersson for the Stokes flow [26] and extended to the Navier–Stokes flow by Gersborg-Hansen et al. [27] and Olesen et al. [28], an artificial friction force is added to the Navier–Stokes equations. This method evolves the artificial porous material to solid and liquid phases which have sufficient high and zero impermeability, respectively.

The artificial friction force is implemented via the Darcy force term as $f = -\alpha(\gamma)u$, where α is the impermeability of the artificial porous medium, γ is the design variable, and u is the velocity of the fluidic flow. The design variable γ is bounded in the interval [0, 1], where zero and one correspond to the solid and fluid phases, respectively. The impermeability of the porous medium is interpolated by the design variable γ as [26–28]

$$\alpha(\gamma) = \alpha_{max} q(1-\gamma)/(q+\gamma) \tag{2}$$

where α_{max} is the artificial impermeability of the solid, q is a positive parameter used to tune the convex property of the interpolating equation. In the topology optimization of fluidic flows, α_{max} should be chosen to be a high but finite number to well approximate the solid and ensure the numerical stability simultaneously.

Based on the above description, the optimal topology of a passive micromixer can be obtained by finding the distribution of the design variable γ for the topology optimization problem expressed as [19,20,24]

Finding the minimum of $\sigma(c)$
Subject to the constraints

$$\nabla \cdot [p\mathbf{I} - \eta(\nabla\mathbf{u} + \nabla\mathbf{u}^{\mathrm{T}})] + \rho\mathbf{u} \cdot \nabla\mathbf{u} = \mathbf{f} \tag{3}$$

$$\nabla \cdot \mathbf{u} = 0 \tag{4}$$

$$\nabla \cdot (-\mathrm{D}\nabla c) + \mathbf{u} \cdot \nabla c = 0 \tag{5}$$

where ρ, η, $\mathbf{u}$, $\mathbf{I}$, p, D are the fluid density, viscosity, velocity vector, unit tensor, pressure field, and diffusion coefficient, respectively. For water as the carrier fluid, $\rho = 1000\,\mathrm{kg/m}^3$ and $\eta = 0.001\,\mathrm{Pa\cdot s}$. And the diffusion coefficient D is equal to $10^{-10}\,\mathrm{m}^2/\mathrm{s}$.

At inlet 1 and 2 uniform velocities are specified as

$$\mathbf{u} = U_{01}\mathbf{n} \quad \text{at} \quad \Gamma_{\text{inlet 1}} \tag{6}$$

$$\mathbf{u} = U_{02}\mathbf{n} \quad \text{at} \quad \Gamma_{\text{inlet 2}} \tag{7}$$

Here, U_{01}, U_{02}, and $\mathbf{n} = (n_x, n_y)$ are the magnitude of the velocity of inlet 1, inlet 2, and the normal vector of the surface, respectively. At channel walls, the nonslip condition is imposed

$$\mathbf{u} = \mathbf{0} \quad \text{at} \quad \Gamma_{\text{wall}} \tag{8}$$

At the channel, outlet the ambient pressure and no-traction condition are applied

$$p = 0 \quad \text{at} \quad \Gamma_{\text{outlet}} \tag{9}$$

$$\eta(\nabla\mathbf{u} + \nabla\mathbf{u}^{\mathrm{T}}) \cdot \mathbf{n} = \mathbf{0} \quad \text{at} \quad \Gamma_{\text{outlet}} \tag{10}$$

For the steady convection–diffusion equation, the concentrations at inlets 1 and 2 are specified as

$$c = 1\,\mathrm{mol/m}^3 \quad \text{at} \quad \Gamma_{\text{inlet 1}} \tag{11}$$

$$c = 0\,\mathrm{mol/m}^3 \quad \text{at} \quad \Gamma_{\text{inlet 2}} \tag{12}$$

While the condition of no species flux is imposed at channel walls

$$(c\mathbf{u} - \mathrm{D}\nabla c) \cdot \mathbf{n} = 0 \quad \text{at} \quad \Gamma_{\text{wall}} \tag{13}$$

The boundary condition at the outlet is

$$(\mathrm{D}\nabla c) \cdot \mathbf{n} = 0 \quad \text{at} \quad \Gamma_{\text{outlet}} \tag{14}$$

In our study, the width of the contraction channel H_b is used as the length scale; the mean velocity $\bar{u}$ in the contraction channel is used as the velocity scale, which can be calculated by the flow rate of the channel and the area of the cross plane, $\mu\bar{u}/H_b$ is used as the pressure scale and the contraction at Γ_{inlet1} is used as the contraction scale. So the optimization objective and governing equations are normalized as follows [19,20,24]:
Finding the minimum of

$$\sigma^*(c^*) = \frac{\int_{\Gamma}(c^* - \bar{c}^*)^2}{A^*\bar{c}^{*2}} \tag{15}$$

Subject to the constraints

$$\nabla^* \cdot [p^*\mathbf{I} - (\nabla^*\mathbf{u}^* + \nabla^*\mathbf{u}^{*\mathrm{T}})] + \mathrm{Re}\mathbf{u}^* \cdot \nabla^*\mathbf{u}^* = -\alpha^*(\gamma)u^* \tag{16}$$

$$\nabla^* \cdot \mathbf{u}^* = 0 \tag{17}$$

$$\nabla^* \cdot (-\mathrm{D}^*\nabla^*c^*) + \mathbf{u}^* \cdot \nabla^*c^* = 0 \tag{18}$$

where the Reynolds number $\mathrm{Re} = \rho\bar{u}H_b/\eta$. And the corresponding boundary conditions are as follows:

$$\mathbf{u}^* = (U_{01}/\bar{u})\mathbf{n} \quad \text{at} \quad \Gamma_{\text{inlet 1}} \tag{19}$$

$$\mathbf{u}^* = (U_{02}/\bar{u})\mathbf{n} \quad \text{at} \quad \Gamma_{\text{inlet 2}} \tag{20}$$

$$\mathbf{u}^* = \mathbf{0} \quad \text{at} \quad \Gamma_{\text{wall}} \tag{21}$$

$$p^* = 0 \quad \text{at} \quad \Gamma_{\text{outlet}}, \\ (\nabla^*\mathbf{u}^* + \nabla^*\mathbf{u}^{*\mathrm{T}}) \cdot \mathbf{n} = \mathbf{0} \quad \text{at} \quad \Gamma_{\text{outlet}} \tag{22}$$
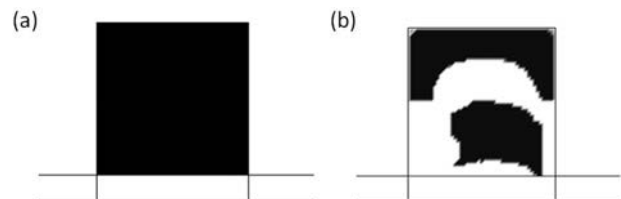

Fig. 2 The structure of the design domain for the simulation (*a*) before and (*b*) after optimization. Initially rigid domain, shown in solid black, is partially converted to fluid channel, shown in white, through optimization process.

$$c^* = 1 \quad \text{at} \quad \Gamma_{\text{inlet1}} \tag{23}$$

$$c^* = 0 \quad \text{at} \quad \Gamma_{\text{inlet2}} \tag{24}$$

$$(c^*\mathbf{u}^* - D^*\nabla^* c^*) \cdot \mathbf{n} = 0 \quad \text{at} \quad \Gamma_{\text{wall}} \tag{25}$$

$$(D^*\nabla c^*) \cdot \mathbf{n} = 0 \quad \text{at} \quad \Gamma_{\text{outlet}} \tag{26}$$

In this optimization, the manufacturability is considered in order to make the mixer be one layer geometry. So an additional manufacturing constraint is added: the design variable should have a consistent value in the depth direction of the design domain [24]. In our problem (Fig. 1), the depth direction is the z axis direction and the same design variable value is applied to the node of the finite element method (FEM) with same x and y coordinates. After that, the distribution of the design variable is transferred to be a function defined in the xy plane. By this, we reduce the number after the FEM discretization.

Furthermore, the spatial periodic layout is considered too, as the series-wound method can be used to obtain the micromixer after one period of the layout for a micromixer is designed. So the periodic constraint is added in order to obtain a micromixer with a spatial periodic layout

$$\gamma(x_0^*) = \gamma(x_0^* + L_p^* i), \quad x_0 \in \Omega_0, \quad i = 1, 2 \cdots m - 1 \tag{27}$$

Here, Ω_0 is the first period and m is the number of periods.

2.2 Computational Method. The expansion channel is specified as the optimization domain, as shown in Figs. 1 and 2(a). The solid and fluid domains are distinguished as black and gray colors, respectively. To obtain the result of the topology optimization, the gradient-based iterative approach is used to implement the optimization process. The method of moving asymptotes (MMA) optimization algorithm is used to implement iteration of numerical optimization [28].

In order to solve the optimization problem based on Eqs. (15)–(27), the fluid field, the concentration field, and sensitivity should be solved. In order to obtain the sensitivity, the adjoint method is used. In this paper, the Navier–Stokes equations and the convection–diffusion equation are solved by the FEM, which are stabilized by the generalized least squares and the streamline upwind Petrov–Galerkin (SUPG) technologies, respectively [29]. So we get the adjoint equation for the stabilized convection–diffusion equation and Navier–Stokes equations in weak form

$$\int_{\Omega} \left(\lambda_{c^*}(\mathbf{u} \cdot \nabla \widehat{\lambda}_{c^*}) + D\nabla \lambda_{c^*} \cdot \widehat{\lambda}_{c^*} \right) d\Omega$$
$$+ \int_{\Omega} (\mathbf{u}^* \cdot \nabla \lambda_{c^*}) \tau_{\text{SUPG}} (\mathbf{u}^* \cdot \nabla \widehat{\lambda}_{c^*} - D\nabla^2 \widehat{\lambda}_{c^*}) d\Omega \tag{28}$$
$$+ 2\int_{\Gamma_{\text{outlet}}} \widehat{\lambda}_{c^*} \frac{(c^* - \bar{c}^*)}{A^*\bar{c}^*2} d\Gamma = 0$$

$$\int_{\Omega} [\nabla \lambda_{\mathbf{u}^*} \cdot (\widehat{\lambda}_{\mathbf{u}^*} + \widehat{\lambda}_{\mathbf{u}^*}^{\mathrm{T}}) - \lambda_{p^*}(\nabla \cdot \widehat{\lambda}_{\mathbf{u}^*})$$
$$+ \lambda_{\mathbf{u}^*}(\widehat{\lambda}_{\mathbf{u}^*} \cdot \mathrm{Re}\nabla \mathbf{u}^* + \mathbf{u}^* \cdot \rho\nabla \widehat{\lambda}_{\mathbf{u}^*}) + \widehat{\lambda}_{\mathbf{u}^*} \alpha^*(\gamma)\widehat{\lambda}_{\mathbf{u}^*}] d\Omega$$
$$- \int_{\Omega} \widehat{\lambda}_{p^*}(-\nabla \cdot \widehat{\lambda}_{\mathbf{u}^*} d\Omega + \sum \int_{\Omega} \tau_{\text{GLS}}(\nabla \lambda_{p^*} \cdot \nabla \widehat{\lambda}_{p^*}) d\Omega$$
$$= -\int_{\Omega} \lambda_{c^*}(\widehat{\lambda}_{\mathbf{u}^*} \cdot \nabla c^*)\widehat{\lambda}_{\mathbf{u}^*} d\Omega$$
$$- \int_{\Omega} \left(\frac{\partial \tau_{\text{SUPG}}}{\partial \mathbf{u}^*} \widehat{\lambda}_{\mathbf{u}^*} \right) \mathbf{u}^* \cdot \lambda_{c^*}(\mathbf{u}^* \cdot \nabla c^* - D\nabla^2 c^*) d\Omega$$
$$- \int_{\Omega} \tau_{\text{SUPG}}(\widehat{\lambda}_{\mathbf{u}^*} \cdot \nabla \widehat{\lambda}_{c^*} - D\nabla^2 c^*) + \mathbf{u}^* \cdot \nabla \widehat{\lambda}_{c^*}(\widehat{\lambda}_{\mathbf{u}^*} \nabla c^*) d\Omega$$
$$\tag{29}$$

Here, $\lambda_{c^*}, \lambda_{p^*}$, and $\lambda_{\mathbf{u}^*}$ are the adjoint variables of c, p, and $\mathbf{u}$, respectively; $\widehat{\lambda}_{c^*}, \widehat{\lambda}_{p^*}, \widehat{\lambda}_{\mathbf{u}^*}$ are the test functions of $\lambda_{c^*}, \lambda_{p^*}$, and $\lambda_{\mathbf{u}^*}$; τ_{SUPG} and τ_{GLS} are the stabilization parameters choosing as in Ref. [29].

Based on the equation above, the adjoint sensitivity of the optimization problem is the following:

$$\frac{D\sigma^*}{D\gamma} = \frac{\partial \alpha}{\partial \gamma} \mathbf{u} \cdot \lambda_{\mathbf{u}^*} \tag{30}$$

The detailed procedure for an iterative optimization includes the following steps: (a) the Navier–Stokes equations and convection–diffusion equation are solved by the FEM after giving the initial value of the design variable γ; (b) the adjoint equations are solved, and then the adjoint derivative and the corresponding objective value are computed; (c) the design variable is updated by the MMA after the adjoint derivative is smoothed; (d) check if the optimization is converged, if not, go to (a); if the stopping conditions are satisfied, and then go to next step (e) post process the final result.

All the numerical discretizations are implemented by the FEM using the commercial FEM package COMSOL Multiphysics V3.5 [30],[2] where all the numerical implementation is merely based on the software basic module: COMSOL Multiphysics → partial differential equation (PDE) modes → PDE, general form. The PDE modes of COMSOL Multiphysics can solve PDEs of the form

$$\nabla \cdot \mathbf{\Lambda} = \mathbf{F} \tag{31}$$

$$-\mathbf{n} \cdot \mathbf{\Lambda} = \mathbf{G} + \left(\frac{\partial \mathbf{R}}{\mathbf{u}} \right)^{\mathrm{T}} \lambda, \quad \mathbf{R} = \mathbf{0} \quad \text{at} \quad \Gamma_{\text{all}} \tag{32}$$

where $\mathbf{\Lambda}$ is the matrix; $\mathbf{F}$, $\mathbf{G}$, and $\mathbf{R}$ are vectors; $\mathbf{n}$ is the unit vector; Γ_{all} is the all boundaries. For this case, the Navier–Stokes equations can be solved by setting

$$\mathbf{\Lambda} = \begin{pmatrix} -2\frac{\partial u^*}{\partial x^*} + p^* & -\left(\frac{\partial u^*}{\partial y^*} + \frac{\partial v^*}{\partial x^*}\right) \\ -\left(\frac{\partial u^*}{\partial y^*} + \frac{\partial v^*}{\partial x^*}\right) & -2\frac{\partial v^*}{\partial y^*} + p^* \\ 0 & 0 \end{pmatrix} \tag{33}$$

$$\mathbf{F} = \begin{pmatrix} -\alpha^* u^* - \mathrm{Re}\left(u^*\frac{\partial u^*}{\partial y^*} + v^*\frac{\partial v^*}{\partial x^*}\right) \\ -\alpha^* v^* - \mathrm{Re}\left(v^*\frac{\partial u^*}{\partial y^*} + u^*\frac{\partial v^*}{\partial x^*}\right) \\ -\left(\frac{\partial u^*}{\partial x^*} + \frac{\partial v^*}{\partial y^*}\right) \end{pmatrix} \tag{34}$$

$$\mathbf{R} = \begin{pmatrix} (u^* - U_{01 \text{ or } 02}/\bar{u})n_x \\ (u^* - U_{01 \text{ or } 02}/\bar{u})n_y \\ 0 \end{pmatrix} \quad \text{at} \quad \Gamma_{\text{inlet 1 or 2}} \tag{35}$$

$$\mathbf{G} = \begin{pmatrix} 0 \\ 0 \\ 0 \end{pmatrix} \quad \text{at} \quad \Gamma_{\text{inlet1or2}} \tag{36}$$

$$\mathbf{R} = \begin{pmatrix} 0 \\ 0 \\ 0 \end{pmatrix} \quad \text{at} \quad \Gamma_{\text{others}} \tag{37}$$
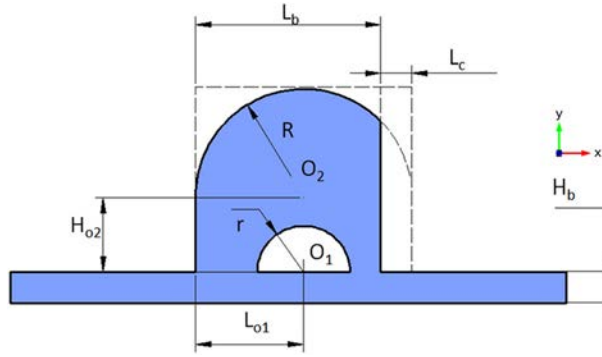
Fig. 3 Lateral structure. *R* and *r* are the radii of the semicircles centered at O_1 and O_2, respectively. L_{o1} is the position of center of semicircles in *x* direction, and $L_{o1} = R = 1/2\, L_a$. L_b and L_c are widths of two rectangles, and $L_b + L_c = 2R$. H_{o1} depicts the position of O_2 and the height of the small rectangle. H_b is the width for the contraction channel.

$$\mathbf{G} = \begin{pmatrix} 0 \\ 0 \\ 0 \end{pmatrix} \quad \text{at} \quad \Gamma_{\text{others}} \tag{38}$$

Similarly, the convection–diffusion equation and the adjoint equations can be solved by PDE, General Form

3 Results

3.1 The Simplified Lateral Structure. In the optimization process, the geometrical parameters of the CEA [19] are set to be $H_a = L_a = L_p = 340\,\mu$m, $H_b = 50\,\mu$m, $D = 50\,\mu$m, $m = 3$. A representative case of an optimized structure for Re $= 50$ is shown in Fig. 2(*b*). We note that one lateral channel is connected to the main channel, instead of only one expansion domain. First there is a bent channel connected to the main channel with an identical width. The width then decreases gradually, generating an impact
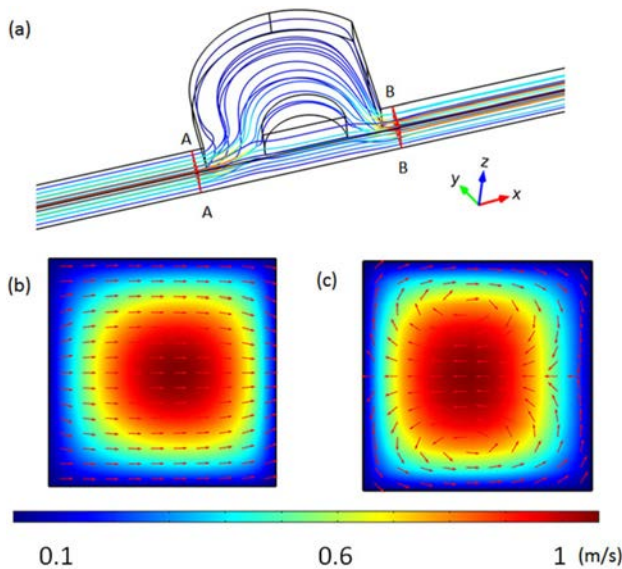

Fig. 4 (*a*) The streamline. The color denotes the velocity. The cross plane A-A is 20 μm from the inlet to lateral structure, B-B cross plane is about 20 μm to the outlet of lateral structure. The velocity field and the (*v, w*) arrow plot of the cross planes (*b*) A-A and (*c*) B-B.
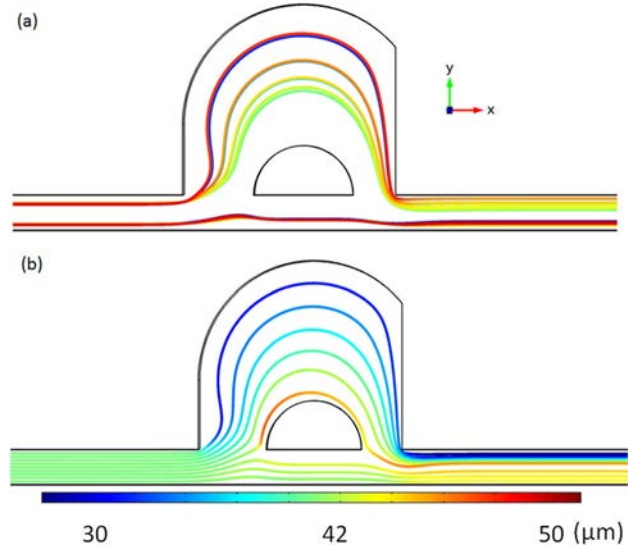
Fig. 5 Streamlines in (*a*) *y* direction with distance from the wall of 10 μm, 1/5 of channel width (*b*) *z* direction with distance from the bottom of 50 μm, 4/5 of channel depth, the color denotes the distance from the wall in *z* direction above

force toward the main flow when the flow in the lateral channel converges to the main channel. Besides, the shape of the optimization result is rather complicated, and will not allow easy fabrication or replication. Like many practices of structure topology optimization, the shape is thus further adjusted for convenience in fabrication [31]. Here we adjust the shape of the result in order to make the shape more regular and propose a lateral structure without changing the topology of the result, as shown in Fig. 3, which is obtained through the Boolean operation of simple geometries: one semicircle and one rectangle union followed by subtraction of one semicircle and two rectangles.

For this lateral structure, we set $R = 1/2L_a = 170\,\mu$m and $H_{02} = 100\,\mu$m to make the design more straightforward and to reduce the space of lateral structure. So, $L_{o1} = 170\,\mu$m. Then we use the parameter sweeping method to design L_c and r. The boundary constraint of L_c and r is $L_c \geq 50\,\mu$m, $r \geq 50\,\mu$m, R-L_c-$r \geq 50\,\mu$m. Through the parameter sweeping we reach $L_c = 50\,\mu$m, $r = 70\,\mu$m.
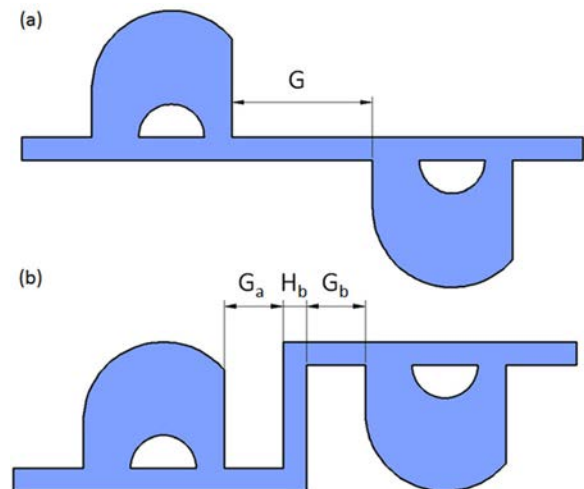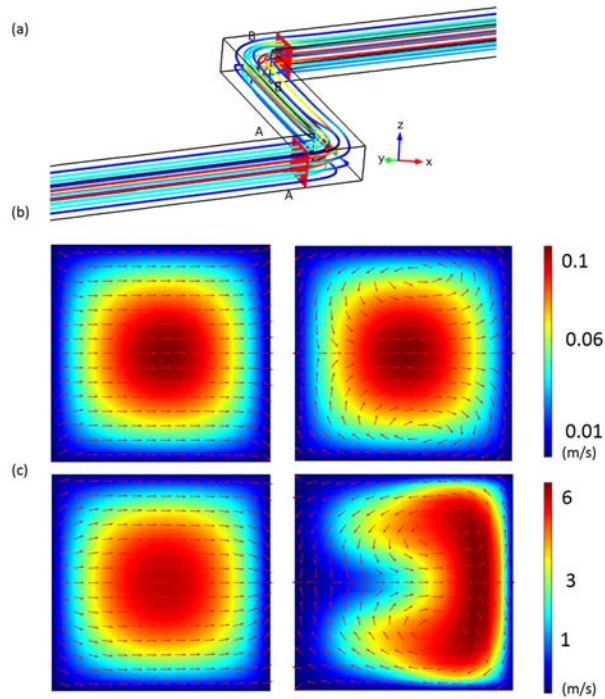

Fig. 6 Arrangement of lateral structures (*a*) in two sides, *G* denotes the distance between the periodic structures. (*b*) The serpentine structures, H_b, denote the width of the turning, same as the width of main channel. Here, $G_a = G_b$, $G_a + G_b + H_b = G$.
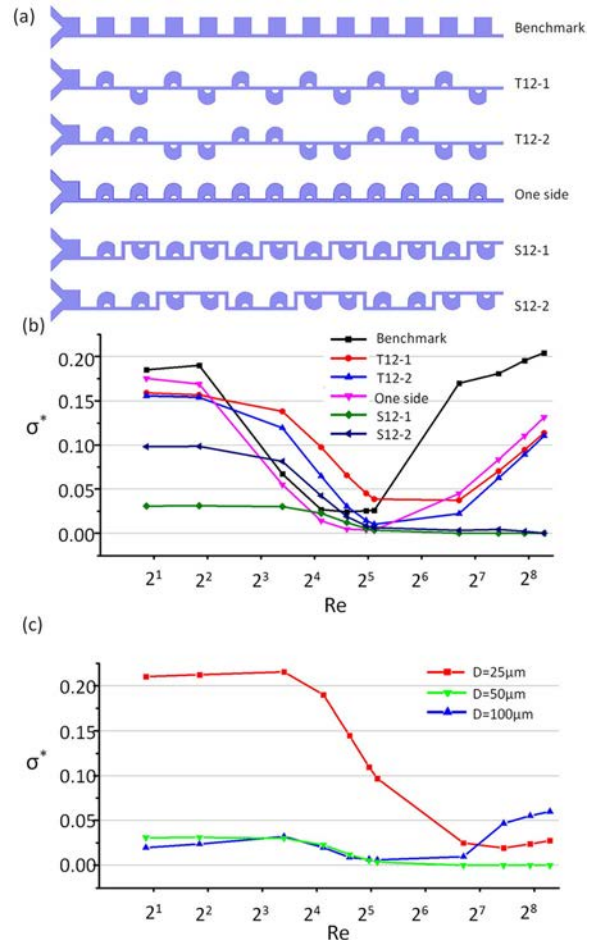
Fig. 7 (*a*) The streamlines in the turning. The cross planes A-A and B-B to the turning is about 20 μm. The velocity field and (*v, w*) arrow plot for the cross planes A-A and B-B with (*b*) Re = 5 and (*c*) 150.

Fig. 8 (*a*) The arrangement of the lateral structure for the mixer. The benchmark is the original contraction–expansion mixer. T12-1 and T12-2 denote the chips with structures arranged in two sides for the period with one and two lateral structures. One side corresponds to the chip with all the lateral structures in the same side. S12-1 and S12-2 denote serpentine structure with a period of one and two lateral structures. (*b*) Mixing efficiency of chips with different arrangements versus Reynolds number, Re, compared against the contraction–expansion chip before optimization. (*c*) Mixing efficiency of chips with different depth versus Reynolds number, Re.

3.2 The Mixing Principle.

The fluid flow will bifurcate at the intersection of the main channel and the lateral structure, with approximately half of the flow rate into the lateral channel (Fig. 4(*a*)). The flow into the lateral channel is accompanied by a weak Dean vortex before the entrance, as the flow is spitted [15,19]. The vortex will generate a secondary flow in the cross plane, as in Fig. 4(*b*). After the fluid enters the lateral channel, there exists another vortex generation because of the inertia of fluid, contraction–expansion structure and semicircular lateral structure [16]. As the fluid leaves the lateral structure, the channel width decreases slowly. So the fluid in the lateral channel is pushed toward the main channel. Therefore, there exists yet another vortex generation, as shown in Fig. 4(*c*). Here we use streamlines to depict the effect of these vortices. In Fig. 5, the streamlines, which have same *y* and *z* coordinate values before the entrance into the lateral channel, show deviation in their *y* or *z* coordinate values after they pass through the lateral channel. This deviation will enhance the reagent mixing. This lateral channel thus utilizes the bifurcation and convergence of fluid to generate vortices as well as secondary flows induced by its contraction–expansion structure. An efficient mixer can then be composed by superposing a series of the lateral structure developed.

4 Discussion

4.1 The Arrangement of the Lateral Structure. Figure 5 shows that the streamlines away from the lateral channel are not disturbed much. Therefore, we arrange the lateral structure in two sides, as shown in Fig. 6(*a*). In order to save space for the chip, we connect the lateral structure using the turning, like in Fig. 6(*b*). The width of the chip with serpentine arrangement is half the width of the chip with two-side arrangement. Furthermore, the turning will generate vortex to enhance the convection of fluid. At the inlet and outlet of the turning, vortices are generated (Fig. 7). The vortex forces the fluid in the center of channel toward the wall of channel. The turning will enhance the mixing with large

Reynolds numbers because the vortices will be enhanced by the turning as the Reynolds number increases (Figs. 7(*b*) and 7(*c*)).

A comprehensive parametric study is performed in order to determine the arrangement of the lateral structures. A representative case is reported here when the geometrical parameters of a chip are $G = 300\,\mu$m, $G_a = G_b = 125\,\mu$m, $H_b = 50\,\mu$m with 12 mixer units present on a chip. The mixing efficiency is calculated based on the concentration of the cross plane 50 μm far from the outlet of the last mixing unit. We choose the following arrangements for the parameter-sweeping study (Fig. 8(*a*)): Benchmark, corresponding to the conventional contraction–expansion chip before optimization, the chips with structures arranged in two sides for the period with one and two lateral structures (T12-1 and T12-2), the chip with all the lateral structures in the same side, the serpentine structures chip with a period of one and two lateral structures (S12-1 and S12-2). After the simulation based on the theory in Sec. 2, we calculate the efficiency based on Eq. (1) as shown in Fig. 8(*b*).

The performance results indicate that the one-side mixer is significantly better than the original contraction–expansion mixer, with the range of Re number for high mixer efficiency of $\sigma^* < 0.0025$ substantially increased. For the Reynolds number of
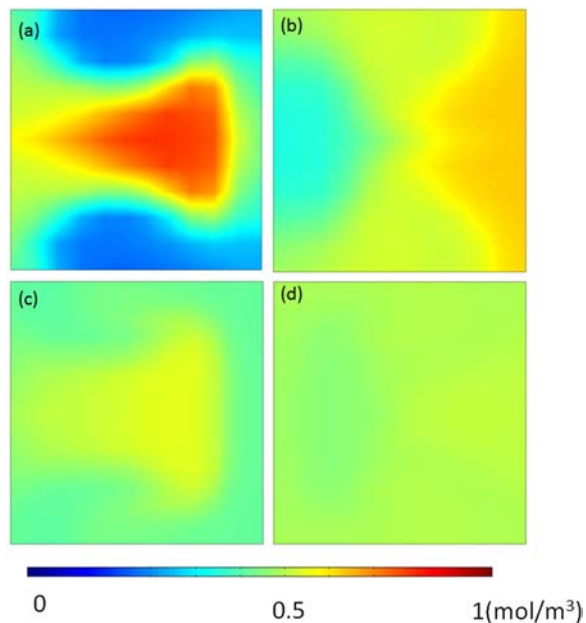
Fig. 9 Mixing efficiency for different number of periods for S12-1 mixer. (a), (b), (c), and (d) represent the cross sections of the first, second, third, and fourth contraction regions after the lateral structure, respectively, for Re = 25.

25, the two reagents are almost completely mixed. However, as seen in Fig. 5, only half of the flow goes through the lateral channel. The lateral channel then will have little effect on the fluid far away from the sidewall of the lateral structure. The curves of T12-1 and T12-2 show that they perform better than the one-side mixer with the increase of the Reynolds number. When the Reynolds number is small mixing can be effectively enhanced by adding more mixer unit to increase the interfacial area between two regents. As the Reynolds number increases, addition of mixer units on the same side cannot be efficient, and so a two-side arrangement must be introduced. For even higher Reynolds numbers, the effect of turning becomes significant, supplementing the
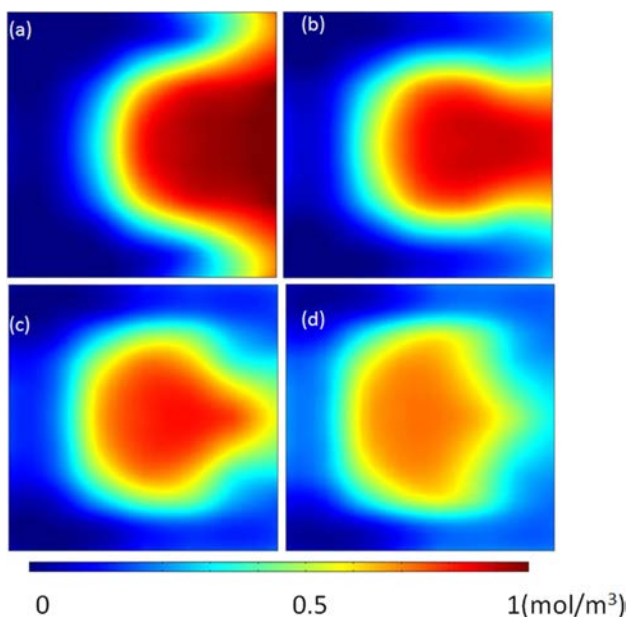
Fig. 10 Mixing efficiency for different number of periods for the original contraction–expansion mixer. (a)–(d) represent the cross sections of the first, second, third, and fourth contraction regions after the expansion structure, respectively, for Re = 25.

effect of the lateral structure. Therefore, judging from the results shown in Fig. 8(b), the serpentine-structure chip with a period of one lateral structure (S12-1) appears to be most robust because it can be used for a wide range of the Reynolds number. Figure 9 shows that the serpentine-structures chip with a period of one lateral structure can make the reagents mixed after a few periods. For Re = 25, the mixing efficiency reaches 0.05 after four periods, indicating that the mixer can be shortened further depending on the Reynolds number, as necessary.

4.2 The Comparison Between the Lateral Structural and the Original Mixer. Figure 9 shows that the serpentine-structures chip with a period of one lateral structure can make the reagents mixed after a few periods. Compared to the mixing process of original contraction–expansion mixer in Fig. 10, the lateral structure first generates the enveloping between two types of reagent in the cross sections of the first contraction region, while the original contraction–expansion mixer generates the enveloping in the third contraction region after the expansion structure. And the center of the fluid core for the lateral structure mixer in the first contraction region is even further than the original mixer. So the mixing effect of the lateral structure is much stronger than the contraction–expansion structure. For example, the mixing efficiency reaches 0.05 after four periods for Re = 25, indicating that the mixer can be shortened further depending on the Reynolds number, as necessary.

However, the lateral structure chip generate mixing when it envelopes one type of reagent by the other, which indicating that the lateral structure is needed to be designed further for the fluid optical fiber, though the focusing efficiency of the structure is higher than the contraction–expansion structure.

4.3 The Aspect Ratio of Channel. The aspect ratio of channel (depth to width) also affects the mixing efficiency. Figure 8(c) shows that the effect of the mixer with low aspect ratio deteriorates for low Reynolds number, weakening the mixing effect of the lateral structure. On the other hand, that with high aspect ratio performs worse with high Reynolds numbers, suggesting that the effect of vortex in the turns are reduced with the increase of the aspect ratio. By using a parameter sweeping method, we confirm that the aspect ratio of one provides best performance as well as convenience in fabrication.

5 Conclusion

A novel one-layer lateral structure mixer, not sensitive to the Reynolds number, is designed through topology optimization, parameter sweeping, and layout designing. The mixing efficiency stays robust for a wide range of the Reynolds number, from 2 to 2^8. The optimization is performed based on conservation laws of mass, momentum, and species, followed by a secondary optimization using Boolean operation of simple geometries for easy fabrication of the resulting lateral structure. A new serpentine mixer then is proposed, composed of turns and these lateral structures. This mixer uses the two structures to generate the Dean vortex, enhancing the fluid convection. It is a one-layer mixer, which can be more easily manufactured by a lithography than multilayer mixers. And also, it is found that serpentine structure with a period of one lateral structure and channel cross section aspect ratio of one is most robust, which is easy to be manufactured.

References

[1] Lee, C.-Y., Chang, C.-L., Wang, Y.-N., and Fu, L.-M., 2011, "Microfluidic Mixing: A Review," Int. J. Mol. Sci., **12**(5), pp. 3263–3287.

[2] Cartier, C. A., Drews, A. M., and Bishop, K. J. M., 2014, "Microfluidic Mixing of Nonpolar Liquids by Contact Charge Electrophoresis," Lab Chip, **14**(21), pp. 4230–4236.

[3] Afzal, A., and Kim, K.-Y., 2012, "Passive Split and Recombination Micromixer With Convergentcdivergent Walls," Chem. Eng. J., **203**, pp. 182–192.

[4] Ammar, H., Ould el Moctar, A., Garnier, B., and Peerhossaini, H., 2014, "Flow Pulsation and Geometry Effects on Mixing of Two Miscible Fluids in Microchannels," ASME J. Fluids Eng., **136**(12), p. 121101.

[5] Karami, M., Shirani, E., Jarrahi, M., and Peerhossaini, H., 2014, "Mixing by Time-Dependent Orbits in Spatiotemporal Chaotic Advection," ASME J. Fluids Eng., **137**(1), p. 011201.

[6] Maki, A.-J., Hemmila, S., Hirvonen, J., Girish, N. N., Kreutzer, J., Hyttinen, J., and Kallio, P., 2014, "Modeling and Experimental Characterization of Pressure Drop in Gravity-Driven Microfluidic Systems," ASME J. Fluids Eng., **137**(2), p. 021105.

[7] Mohammadi, M., and Sharp, K. V., 2013, "Experimental Techniques for Bubble Dynamics Analysis in Microchannels: A Review," ASME J. Fluids Eng., **135**(2), p. 021202.

[8] Sen, A. K., and Bhardwaj, P., 2012, "Microfluidic System for Rapid Enumeration and Detection of Microparticles," ASME J. Fluids Eng., **134**(11), p. 111401.

[9] Solovitz, S. A., Zhao, J., Xue, W., and Xu, J., 2013, "Uniform Flow Control for a Multipassage Microfluidic Sensor," ASME J. Fluids Eng., **135**(2), p. 021101.

[10] Qian, S., and Bau, H. H., 2002, "A Chaotic Electroosmotic Stirrer," Anal. Chem., **74**(15), pp. 3616–3625.

[11] Qian, S., and Bau, H. H., 2005, "Magneto-Hydrodynamic Stirrer for Stationary and Moving Fluids," Sens. Actuators B, **106**(2), pp. 859–870.

[12] Liang, L., and Xuan, X., 2012, "Diamagnetic Particle Focusing Using Ferromicrofluidics With a Single Magnet," Microfluid. Nanofluid., **13**(4), pp. 637–643.

[13] Wen, C.-Y., Liang, K.-P., Chen, H., and Fu, L.-M., 2011, "Numerical Analysis of a Rapid Magnetic Microfluidic Mixer," Electrophoresis, **32**(22), pp. 3268–3276.

[14] Cardoso, V. F., Knoll, T., Velten, T., Rebouta, L., Mendes, P. M., Lanceros-Mendez, S., and Minas, G., 2014, "Polymer-Based Acoustic Streaming for Improving Mixing and Reaction Times in Microfluidic Applications," RSC Adv., **4**(9), pp. 4292–4300.

[15] SadAbadi, H., Packirisamy, M., and Wuthrich, R., 2013, "High Performance Cascaded pdms Micromixer Based on Split-and-Recombination Flows for Lab-On-A-Chip Applications," RSC Adv., **3**(20), pp. 7296–7305.

[16] Amini, H., Lee, W., and Di Carlo, D., 2014, "Inertial Microfluidic Physics," Lab Chip, **14**(15), pp. 2739–2761.

[17] Zhang, J., Li, W., Li, M., Alici, G., and Nguyen, N.-T., 2014, "Particle Inertial Focusing and Its Mechanism in a Serpentine Microchannel," Microfluid. Nanofluid., **17**(2), pp. 305–316.

[18] Amini, H., Sollier, E., Masaeli, M., Xie, Y., Ganapathysubramanian, B., Stone, H. A., and Di Carlo, D., 2013, "Engineering Fluid Flow Using Sequenced Microstructures," Nat. Commun., **4**, p. 1826.

[19] Lee, M. G., Choi, S., and Park, J.-K., 2009, "Rapid Laminating Mixer Using a Contraction–Expansion Array Microchannel," Appl. Phys. Lett., **95**(5), p. 051902.

[20] Lee, M. G., Choi, S., and Park, J.-K., 2010, "Rapid Multivortex Mixing in an Alternately Formed Contraction-Expansion Array Microchannel," Biomed. Microdevices, **12**(6), pp. 1019–1026.

[21] Lee, M. G., Choi, S., and Park, J. K., 2011, "Inertial Separation in a Contraction–Expansion Array Microchannel," J. Chromatogr. A, **1218**(27), pp. 4138–4143.

[22] Lee, M. G., Shin, J. H., Bae, C. Y., Choi, S., and Park, J.-K., 2013, "Label-Free Cancer Cell Separation From Human Whole Blood Using Inertial Microfluidics at Low Shear Stress," Anal. Chem., **85**(13), pp. 6213–6218.

[23] Liu, Z., Deng, Y., Lin, S., and Xuan, M., 2012, "Optimization of Micro Venturi Diode in Steady Flow at Low Reynolds Number," Eng. Optim., **44**(11), pp. 1389–1404.

[24] Deng, Y., Liu, Z., Zhang, P., Liu, Y., Gao, Q., and Wu, Y., 2012, "A Flexible Layout Design Method for Passive Micromixers," Biomed. Microdevices, **14**(5), pp. 929–945.

[25] Deng, Y., Zhang, P., Liu, Y., Wu, Y., and Liu, Z., 2013, "Optimization of Unsteady Incompressible Navier–Stokes Flows Using Variational Level Set Method," Int. J. Numer. Methods Fluids, **71**(12), pp. 1475–1493.

[26] Borrvall, T., and Petersson, J., 2003, "Topology Optimization of Fluids in Stokes Flow," Int. J. Numer. Methods Fluids, **41**(1), pp. 77–107.

[27] Gersborg-Hansen, A., Sigmund, O., and Haber, R. B., 2005, "Topology Optimization of Channel Flow Problems," Struct. Multidiscip. Optim., **30**(3), pp. 181–192.

[28] Olesen, L. H., Okkels, F., and Bruus, H., 2006, "A High-Level Programming-Language Implementation of Topology Optimization Applied to Steady-State Navier–Stokes Flow," Int. J. Numer. Methods Eng., **65**(7), pp. 975–1001.

[29] Donea, J., and Huerta, A., 2003, *Finite Element Methods for Flow Problems*, Wiley, Hoboken, NJ.

[30] Deng, Y., Liu, Z., Zhang, P., Liu, Y., and Wu, Y., 2011, "Topology Optimization of Unsteady Incompressible Navier–Stokes Flows," J. Comput. Phys., **230**(17), pp. 6688–6708.

[31] Liu, Z., Gao, Q., Zhang, P., Xuan, M., and Wu, Y., 2011, "Topology Optimization of Fluid Channels With Flow Rate Equality Constraints," Struct. Multidiscip. Optim., **44**(1), pp. 31–37.